Understanding instability in formamidinium lead halide perovskites: kinetics of transformative reactions at grain and sub-grain boundaries

Parth Raval, Rhiannon Kennard, Eugenia Vasileiadou, Clayton Dahlman, Ioannis Spanopoulos, Michael Chabinyc, Mercouri Kanatzidis, G. Manjunatha Reddy

Understanding instability in formamidinium lead halide perovskites: kinetics of transformative reactions at grain and sub-grain boundaries

Parth Raval[ǂ], Rhiannon M. Kennard[§], Eugenia S. Vasileiadou[#], Clayton J. Dahlman[§], Ioannis Spanopoulos,[# ¤] Michael L. Chabinyc[§], Mercouri Kanatzidis[#], and G. N. Manjunatha Reddy[#ǂ*]

[ǂ]*University of Lille, CNRS, Centrale Lille, Univ. Artois, UMR 8181- UCCS - Unité de Catalyse et Chimie du Solide, F-59000 Lille, France*

[§]*Materials Department, University of California, Santa Barbara, California 93106, U. S. A.*

[#] *Department of Chemistry, Northwestern University, Evanston, Illinois 60208, U. S. A.*

**Corresponding authors email: gnm.reddy@univ-lille.fr*

Abstract

Transformative and reconstructive reactions impart significant structural changes at particle boundaries of hybrid perovskites, which influence environmental stability and optoelectronic properties of these materials. Here, we investigate the moisture-induced transformative reactions in formamidinium based perovskites $FAPbX_3$ (X=I, Br) and show that the ambient stability of these materials can be adjusted from a few hours to several months. For $FAPbI_3$, roles of water vapor, particle size, and light illumination on the kinetic pathways of the cubic (α) transformation to the hexagonal (δ) phase are analyzed by X-ray diffraction, optical microscopy, photoluminescence and solid-state NMR spectroscopy techniques. The grain and sub-grain boundaries exhibit different $\alpha \rightarrow \delta$-$FAPbI_3$ phase transformation kinetics. Our study suggests that the dynamic transformation involves the local water-induced dissolution of the cubic phase

occurring at the crystal surfaces followed by precipitation of the hexagonal phase. Insights into structures and dynamics of a kinetically trapped α|δ-$FAPbI_3$ are obtained by ^{1}H, ^{2}H, and ^{207}Pb ssNMR spectroscopy.

TOC graphic

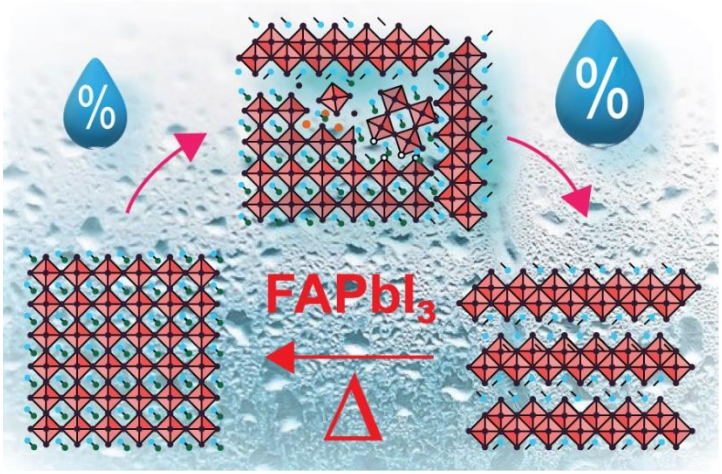

Metal halide perovskites (MHPs) are attractive for many applications in optoelectronics, photovoltaics, photocatalysis, laser, and display technologies due to their intriguing optoelectronic properties.[1–3] Despite the merits of MHPs, such as low cost fabrication and excellent optoelectronic properties,[4–7] these materials are notorious for their "volatile" chemistry with respect to external stimuli such as light, moisture, pressure, and temperature.[8–10] Much research is therefore focused on improving the environmental stability of MHPs: strategies include compositional and dimensional tailoring,[11] defect passivation, additive, and interfacial engineering approaches.[12–14]

Perovskite formulations containing formamidinium (FA) cation exhibit enhanced thermal stability, paving the way towards stable and efficient formulations that are also among the highest performing perovskite solar cells today.[15–20] Encouraged by this progress, efforts to address the

long-term stability with respect to the rigorous standards of the damp heat test (International Electrotechnical Commission IEC-61646 stability assessment at 85 °C and 85% relative humidity in the air for over 1000 h) is at the forefront of hybrid perovskites research.[21,22] To date, these tests have been done on FA-based alloy compositions used in solar cells: methylammonium-formamidinium lead bromide-iodide (MA, FA)Pb(Br, $I)_3$, (Cs, FA)Pb(Br, $I)_3$ and (Cs, MA, FA)PbI_3.[23–25] Within the recent past, much efforts have been expended to the stabilization of black(α)-$FAPbI_3$ phase using additive and interfacial engineering strategies that lead to stable and efficient photovoltaic cells.[12,13,15,26–31] However, in order to understand how to further improve the stability of such alloys and neat formulations, we must first understand the transformative reactions and degradation of the reference compounds with single-cation/single-anion compositions, $FAPbI_3$ and $FAPbBr_3$. We, therefore, turn our attention to these two compositions, with particular attention paid to $FAPbI_3$, as this composition is known to be less stable at near ambient temperatures.[32,33]

The dynamic interface between corner-sharing lead halide octahedra and organic cations is thought to affect the instability in perovskites, which further depends on compositions and other external stimuli that lead to structural deterioration and point defects. For $FAPbI_3$, the metastable black cubic phase (α) converts to the yellow hexagonal phase (δ) at ambient temperatures.[34,35] The transition $\alpha \rightarrow \delta$ $FAPbI_3$ occurs through various intermediate stages, separated by a free energy barrier of the order of hundreds of meV. This barrier results in a large thermal hysteresis between the $\delta \rightarrow \alpha$ transition occurring at 350 K, whereas the $\alpha \rightarrow \delta$ transition occurring at 290 K, and explains at least in part, how the α-$FAPbI_3$ can be kinetically trapped at ambient temperature.[35] Several *in situ* and *ex-situ* characterization techniques have been used to study phase stability in FA-based and FA-rich perovskites.[10,30,36] It has been suggested that the grain boundaries are susceptible to water-ingress, leading to $\alpha \rightarrow \delta$ phase transformation.[37] However, this reaction is

reported to endure between hours to months to complete, as different studies report the different synthetic, fabrication, and aging conditions.[38–40] In addition, photo thermal induced resonance (PTIR with a spatial resolution of ~100 nm) and time-of-flight secondary ion mass spectrometry (TOF-SIMS) techniques have been employed to characterize the humidity-induced phase transformations and to probe surface and sub-surface compositions in FA-rich perovskites.[41] Solid-state NMR (ssNMR) spectroscopy is a local probe that provides information on the structures and dynamics in hybrid perovskites with site-specificity: for example, ssNMR techniques have been used to gain insight into chemical doping, cation-ordering and dynamics, interfacial engineering, phase stability, and degradation products.[42–48] However, a precise understanding of how water molecules induce a "catalysis-like" transformative reaction, i.e., how water reacts without directly integrating into the initial perovskite (α) or the final non-perovskite (δ) $FAPbI_3$ structures, and insight into the nature of the intermediate phase(s) is lacking, which necessitates further investigation. Because this reaction contributes to the $FAPbI_3$ instability that rigorously affects the performance of solar cells, it is crucially important to understand the molecular origins of the phase transition, kinetic and thermodynamic factors, which influence the degradation of hybrid perovskites.[49]

Here, we examine the α→δ $FAPbI_3$ transformative reaction triggered by moisture as a function of particle size, concentration of water vapor in the air, and laboratory light illumination. The transformative reactions are characterized at different length scales using X-Ray Diffraction (XRD), optical microscopy, photoluminescence, and ssNMR spectroscopy techniques. Specifically, local chemical environments of organic cations and lead octahedra in black (α), yellow (δ), and intermediate (α|δ) phases are analyzed by 1D ^{1}H, ^{2}H, ^{207}Pb, and 2D ^{1}H-^{1}H and ^{1}H-^{207}Pb ssNMR spectroscopy. The reaction kinetics, rate constants and half-lives were measured and

compared for the black $FAPbI_3$ particles exposed to moisture at different conditions and durations. We then introduce on-the-fly deuteration approach of NH_2 sites in FA^+ cations to capture the different dynamic behaviors of FA^+ cations in the intermediate phases. The α–$FAPbI_3$ exhibits excellent air stability for several months at ambient temperatures and at 40% RH. However, it transforms into δ–$FAPbI_3$ within a few days upon exposure to moisture at 80% RH, whereby the laboratory illumination further accelerates this transformation. In contrast to $FAPbI_3$, $FAPbBr_3$ particles show enhanced moisture stability over a range of moisture exposure conditions, which indicates choice of halogen atom plays a significant role in governing the environmental stability of hybrid perovskites.

Figure 1 shows the cubic (α) to hexagonal (δ) phase transition in bulk crystals as observed by powder X-Ray Diffraction (XRD), photoluminescence (PL), and solid-state ^1H and ^{207}Pb NMR spectroscopy. For XRD, the close match in peak locations and intensities between the simulated and experimental XRD patterns (Supporting Information, SI, Figure S1) indicates that the powders of the α and δ phases are phase-pure in bulk.[7,50] For the $FAPbI_3$ after 8h of hydration (100% RH), the characteristic (100) peak of the delta phase appears near 12°, and the transformation is complete after 21h (Figure 1a). To examine the moisture stability required for the IEC 61646 damp heat test, we then acquired XRD patterns of the same $FAPbI_3$ material as a function of exposure time to moisture at 85% RH (SI, Figure S2), which indicates that the complete α→δ $FAPbI_3$ transformation takes longer than 2 days to complete. These two stability tests confirm that the water vapor in the air has a detrimental effect on the ambient stability α–$FAPbI_3$ phase. These results are corroborated by the PL studies (Figure 1b) of neat α–$FAPbI_3$ phase that shows a strong PL intensity peak at 790 nm and a weaker PL intensity (non-normalized) for the intermediate phase

(85% RH, 15h of exposure) and no PL intensity for the hexagonal phase after 45h of exposure to moisture.

To examine the cubic (α) to hexagonal (δ) phase transition more closely, we employed high-field ^{1}H and ^{207}Pb ssNMR spectroscopy. Specifically, the ^{207}Pb chemical shift is sensitive to Pb-I distances, apical Pb-I-Pb bond angles, and distortions in lead iodide octahedra.[48,51–53] 1D ^{207}Pb magic-angle spinning (MAS) spectra of black, intermediate, and yellow $FAPbI_3$ crystals (Figure 1c) exhibit different signals, whereby the signal centered at ~1556 ppm in the fresh $FAPbI_3$ corresponds to Pb atoms in cubic phase (α-$FAPbI_3$). The same material upon exposure to moisture (85±5% RH, 20h) exhibited two well-resolved ^{207}Pb signals at ~1556 and ~1164 ppm, which are attributable to two distinct ^{207}Pb local environments in the cubic and hexagonal phases. After exposure to 85±5% humidity for 45h, only the peak near ~1164 ppm is present, which confirms that this peak corresponds to the hexagonal phase. The low-frequency shift of ^{207}Pb peak near 1164 ppm indicates octahedral tilting, consistently with previous ^{207}Pb assignments.[51–53] While ^{1}H MAS NMR spectrum (Figure 1d) of the black phase displays signals associated with –CH (8.1 ppm) and $–(NH_2)_2$ groups (7. 4 ppm) of FA^+ cations, additional signals corresponding to –CH (8.5 ppm) and $–(NH_2)_2$ groups (7.6 ppm) of FA^+ cations in the yellow phase have emerged after 5h of exposure to moisture and complete conversion into the yellow phase occurs after 45h (~2 days). Notably, high-field ^{1}H MAS NMR (21 T, 900 MHz) improved our resolution abilities to examine reaction kinetics of the α→δ phase transformation, as discussed below.

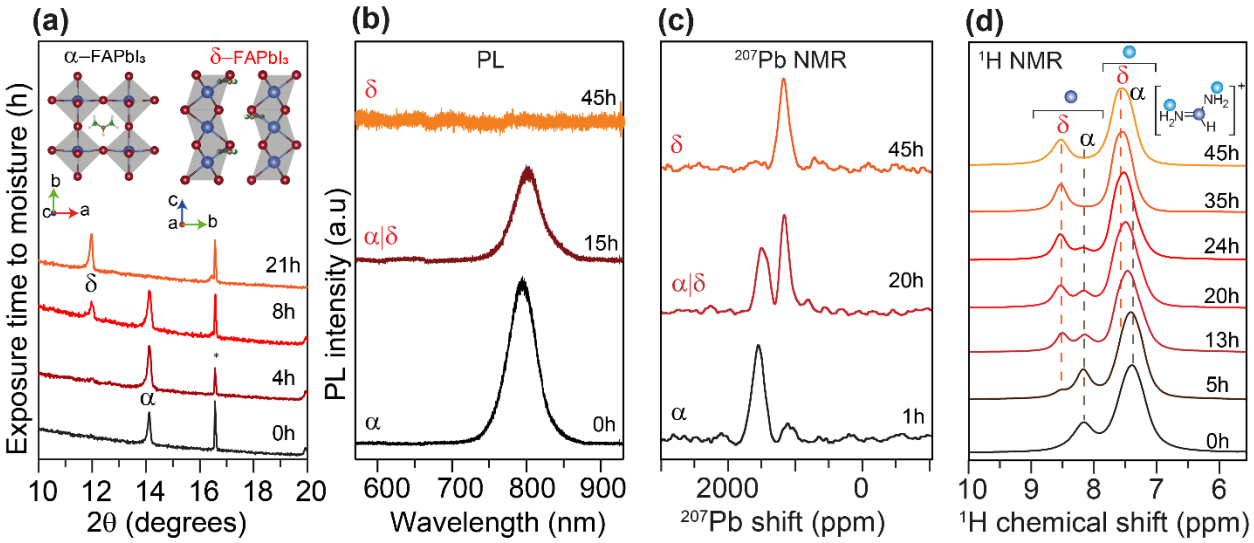

Figure 1. (a) *Ex-situ* XRD patterns of $FAPbI_3$ as a function of moisture (100% RH in the air) exposure time. Peaks near 16.6 degrees correspond to quartz substrates denoted by asterisk and (b) photoluminescence spectra of $FAPbI_3$ as a function of moisture (85% RH) exposure time. 1D (c) ^{207}Pb and (d) ^{1}H MAS NMR spectra of fresh (α-$FAPbI_3$) and aged (α|δ-$FAPbI_3$, δ-$FAPbI_3$) materials upon exposure to moisture (85% RH). Signals associated with α and δ polymorphs are indicated and color-coded as depicted in the schematic structure figure in (d). Crystal structures of α and δ polymorphs are shown in the inset of (a). All ^{1}H (900.2 MHz) and ^{207}Pb (167.6 MHz) spectra were acquired with 50 kHz MAS.

Particle size, light, water vapor, and temperature are among the factors that influence the kinetics of α→δ $FAPbI_3$ transformative reaction. First, we analyze the role of particle size on α→δ phase transformation kinetics catalyzed by moisture (85% RH). The different particle sizes in the 20-100 μm range obtained by different synthesis routes (SI, Materials and methods) were analyzed and compared. The particle size distributions for small (≈32±11 μm) and large (≈74±41 μm) $FAPbI_3$ particles were estimated by analyzing electron micrographs (SI, Figure S3). The α→δ $FAPbI_3$ transition visualized by optical microscopy (SI, Figure S4) suggests that the particle

boundaries populated with the α–$FAPbI_3$ phase (i.e., large surface area of black phase is open for the interaction with water molecules) trigger the transformative reactions at the surface, which then penetrates into the sub-surfaces and to the bulk. Due to different distributions of particle sizes, there is a large heterogeneity in how fast α–$FAPbI_3$ convert into δ–$FAPbI_3$ phase. It is plausible that this heterogeneity in reaction rate depends on the concentration of reactive interfaces at the grain boundaries as well as reactive intra-grain interfaces.[54] Nonetheless, the smaller $FAPbI_3$ particles react with water faster than the larger particles (SI, Figures S5, and S6), due to the high surface area associated with the former, allowing greater interaction with water. Kinetics plots of α→δ phase transformation measured by means of the ^1H signal (–CH site of FA^+, 8.1 ppm) intensity decay in the α phase and the simultaneous buildup of the ^1H signal intensity of the same sites for the δ phase (8.5 ppm) as a function of moisture exposure time can be approximated to the exponential build-up/decay function. A good agreement was observed between the experimental intensity buildup and first-order kinetics model with a co-efficient of determination R^2=0.995 (SI, section 5, Figure S7), and data fitted against this model led to poor agreement. The (pseudo)first-order reaction kinetics suggests that the phase transformation is mediated by "liquid-like" transient species (*vide infra*), indicating the surface-induced dissolution of the black phase followed by a precipitation of the yellow phase. We reasoned that the reaction rate depends on the surface wettability (water vapor concertation) and/or the particle exposure area. This trend is observed for different humidity points and particle sizes, following the (pseudo)first-order kinetics (Figure 2, and Figures S8b,d, S9), whereby a rapid evolution of α→δ phase transformation occurs at an early hydration period. This sudden increase in the formation of the δ–$FAPbI_3$ can be attributed to the susceptible water ingress at the particle boundaries of α–$FAPbI_3$,[55–57] which is consistent with the optical microscopy analysis (SI, Figures S5, and S6). The rate at which the α→δ $FAPbI_3$

transformative reaction occurs can be modeled by the (pseudo)first−order kinetics, which leads to the estimation of rate constants and half-lives of α–$FAPbI_3$ particles (Table 1). When large particles (40-100 μm) are exposed to moisture (85% RH), ~50% of the δ–$FAPbI_3$ is formed in less than 15h, which then rises to over 90% in ~2 days and the complete transformation occurs after several days. Based on the analysis of kinetics plots, the rate constant for this reaction is estimated to be 0.052 h^{-1} with a half-life decay time of ≈13.3h (SI, Table S1). By comparison, smaller α-$FAPbI_3$ particles (20-40 μm) exhibited rapid transformation kinetics (Figure S8c,d) upon exposure to moisture (85% RH) due to the increased water/particle interfacial interaction that accelerates the α→δ $FAPbI_3$ transformation. In this latter case, the rate of transformative reaction was found to be 0.061 h^{-1} and the half-life, $t_{1/2}$ (85% RH, 20-40 μm) is ≈11.4h. It should be noted that the difference between the half-lives ($\Delta t_{1/2}$) for large and small particles is 2h (SI, Figure S9) which is relatively short, due to the non-uniformity in particle sizes, shapes, and overlap between the particle size distributions.

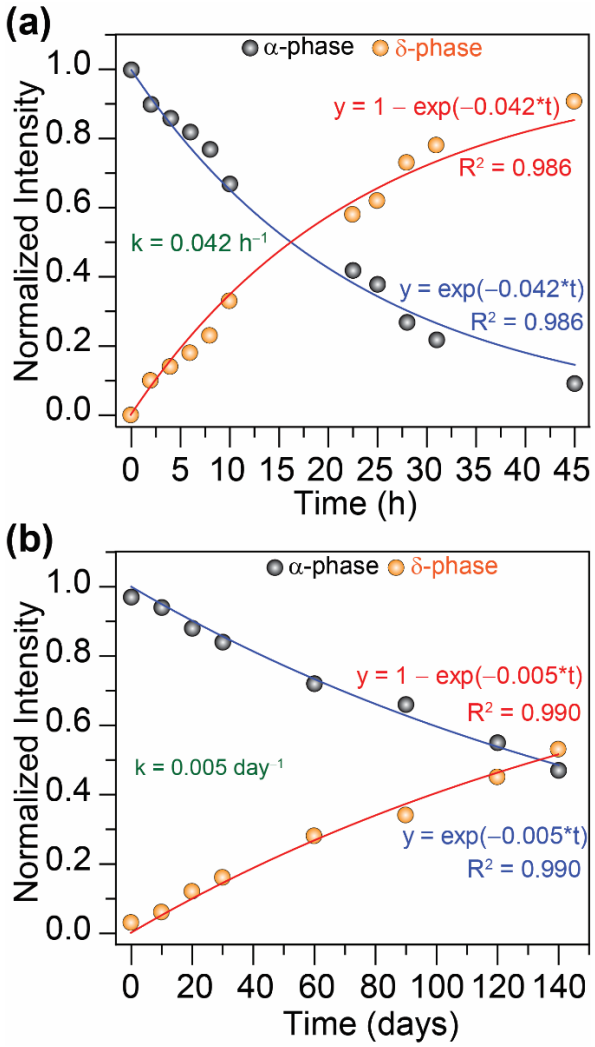

Figure 2. Kinetics plots of ^{1}H signal intensity buildup of -CH sites of FA^{+} cations in δ–$FAPbI_3$ and the simultaneous ^{1}H signal intensity decay for the same sites in α–$FAPbI_3$ as a function of exposure time to moisture in the dark at relative humidity levels (a) 85% RH and (b) 40% RH.

Further insight into the role of external stimuli such as water vapor and light illumination on the reaction kinetics of α→δ transformation can be obtained by analyzing kinetic plots of $FAPbI_3$ obtained from ^{1}H MAS NMR spectroscopy. For small particles (20-40 μm), Figure 2 presents the kinetics of α→δ $FAPbI_3$ phase transition examined at different concentrations of water molecules in the air (85% and 40% RH). Although continuous exposure to water vapor at 85% RH

leads to a α→δ $FAPbI_3$ phase transformation in a few days with a rate constant of $0.042h^{-1}$ (Figure 2a), the same material upon exposure to 40% RH leads to relatively slow transformation with a half-life decay time of 3327 h (~133 days) and the complete transformation is estimated to take up to a year by extrapolating the kinetics plots (Table 1). These results are in line with the optical microscopy analysis (SI, Figures S4-S6), which indeed explains that it would take ≈16.5h of exposure at 85% RH to convert nearly one-half of the α–$FAPbI_3$ into δ–$FAPbI_3$, however, the complete transformation into δ–$FAPbI_3$ takes several days. This is likely due to the much lower water ingression through the particle boundaries that are covered by the yellow phase, thus leading to a sluggish phase transformation of black particles trapped in the sub-surfaces or reactive intra-grain interfaces in $FAPbI_3$ particles. For the large particles of over 100 μm exposed to moisture (40% RH), a complete α→δ $FAPbI_3$ phase transformation is expected to take over a year due to relatively low concentration of water vapor in the air. Trace amounts of surface preabsorbed chemical species such as trapped water, dioxygen, or precursors used in the synthesis process may also contribute to the degradation process.[55] However, the species were not detected either in NMR or XRD experiments, suggesting that any such chemical residues are at minuscule concentrations if present.

Table 1. Half-life decay time associated with α→δ phase $FAPbI_3$ transformation in the dark with varying relative humidity. The particle size distribution is 20-40 μm.

Relative humidity (RH, %)	**Half-life decay time ($t_{½}$, h)**
85	16.5
40	3327

Light illumination is another factor that could contribute to the α→δ–$FAPbI_3$ phase transformation. To test this, we studied the moisture-induced (85% RH) degradation kinetics of small particles (20-40 μm) under dark and laboratory light illumination. The presence of light illumination (500-750 Lux) accelerates α→δ $FAPbI_3$ phase transformation, further reducing the half-lives from 16.5h to 11.4h (SI, Figure S10, and Table S2). We highlight that, despite the excellent thermal stability of the $FAPbI_3$ black phase,[58] the large variation in the kinetics of α→δ $FAPbI_3$ transformation is due to the deleterious effect of water molecules and light illumination combined. The most important takeaway from this study is that the impact of concentration of water vapor, and light illumination on the kinetics of transformative reactions can be disentangled and compared, among which relative humidity in the air seems to play a vital role in governing the environmental stability of optoelectronic devices. For example, it has been shown the $FAPbI_3$-based solar cell efficiency reduces to one-half of its initial value within a few hours upon exposure to moisture (40 °C, 70% RH, 5h, AM 1.5G UV-light illumination), consistently with this study.[59] However, the stability of $FAPbI_3$ and FA-rich thin films depends on various factors such as deposition and annealing conditions, and the encapsulation and passivation strategies further exacerbate the situation. Therefore, an extrapolation of the kinetics plots of the crystals to the thin films in solar cells and other optoelectronic devices is less straightforward. Overall, our study indicates that the large grains are likely to be beneficial for the environmental stability of $FAPbI_3$ and FA-rich perovskite formulations.

The fundamental pertinent question is how the phase transformation occurs at the particle boundaries, and how to resolve the interfacial structure of α|δ-$FAPbI_3$ phase. We sought to understand if there is a significant mixing of cubic and hexagonal phases during the transformation

and any amorphous phases, as XRD shows only the reflections corresponding to α and δ phases, and as optical microscopy suggests lack of intermixed α and δ phases (Figures 3a, S6). Previous studies suggested that the thermal transformations in lead halide perovskites occur through liquid-like interfaces.[60] The liquid-like behavior indeed facilitates surface reactions in order to modulate hybrid perovskite structures and properties.[61] Understanding the chemical nature of an intermediate phase at short-length scales (< 1 nm) is expected to cast light on the surface/interfacial reactions that cause perovskite degradation. A schematic of α→δ transformation with plausible intermediate products based on the optical microscopy analysis is shown in Figure 3a,b, and 2D ^{1}H-^{207}Pb, and ^{1}H-^{1}H correlation spectra of partially transformed $FAPbI_3$ particles (aged for 24 h at 85% RH) are presented in Figure 3c-e. In particular, optical microscopy images of α|δ-$FAPbI_3$ particles (Figure 3a) formed during the phase transition show distinct morphological features indicating the presence of yellow and black $FAPbI_3$ domains. By analyzing the 2D ^{207}Pb-^{1}H correlation spectrum of the same α|δ-$FAPbI_3$ phase (Figure 3c), through-space sub-nanometer ^{207}Pb-^{1}H proximities between FA^+ and PbI_6 octahedra at the organic-inorganic interface are distinguished and identified: 2D peaks at 1556 ppm (^{207}Pb) and 7.4 and 8.1 ppm (^{1}H) correspond to the organic-inorganic interface in α–$FAPbI_3$, and low-intensity signals between ^{207}Pb (1556 ppm) and ^{1}H (7.6 and 8.5 ppm) sites indicate that the through-space proximities between α– and δ-$FAPbI_3$ moieties. It can be hypothesized that the minuscule concentrations of $[PbI_6]^{4-}$, $[Pb(H_2O)_6]^{2+}$, $[PbI_2.4H_2O]$ $[PbI_3.3H_2O]^-$ $[PbI_4.2H_2O]^{2-}$ complexes may exist at the interface during the phase transformation, although undetected in both XRD and ssNMR experiments. Insight into the organic-organic interface can be obtained by analyzing ^{1}H-^{1}H correlation spectra (Figure 3d,e).

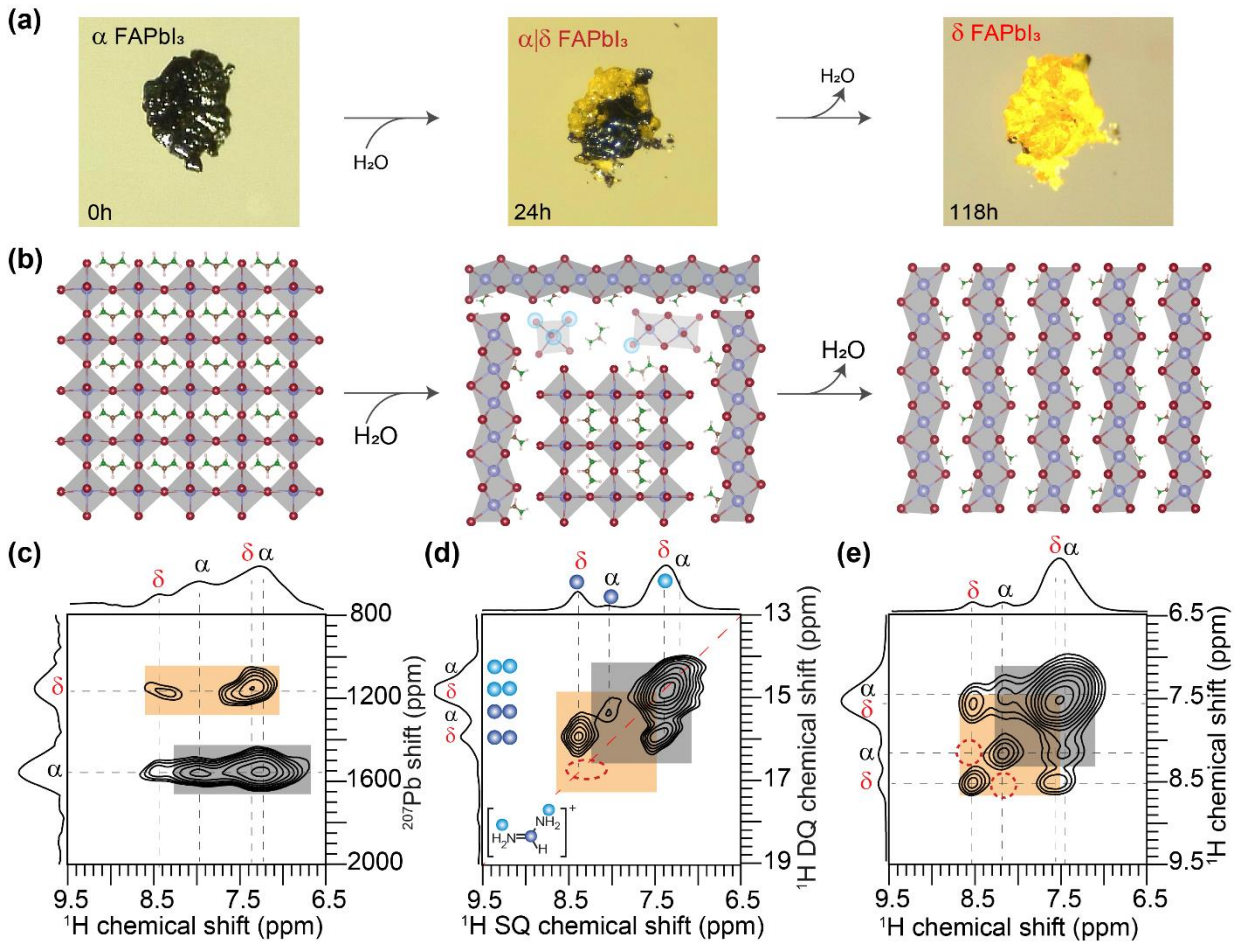

Figure 3. (a) High-resolution optical microscopy images of fresh and aged (after exposure to moisture) $FAPbI_3$ particles. (b) Schematic of α→δ $FAPbI_3$ transformation upon exposure to moisture. Solid-state 2D ssNMR spectra of α|δ-$FAPbI_3$ phase obtained after exposure to moisture (24 h, 85% RH): (c) ^{1}H-^{207}Pb heteronuclear correlation acquired with 6 ms of cross-polarization contact time, (d) ^{1}H-^{1}H DQ–SQ correlation and (e) ^{1}H-^{1}H spin-diffusion, acquired at room temperature and at 21 T (^{1}H 900.2 MHz) with 50 kHz MAS. The corresponding skyline projections are shown along the top ^{1}H SQ horizontal axis. Correlated signal intensities originating from dipolar-coupled ^{1}H-^{1}H pairs are depicted by colored circles. In (c-e), 2D peaks depicted in gray and yellow boxes correspond to the black and yellow $FAPbI_3$ phases, and the dashed red circles indicate the absence of dipolar interactions between the FA^{+} cations in these two phases.

In a 2D ^{1}H-^{1}H Double-Quantum-Single-Quantum (DQ-SQ) correlation NMR experiment, 2D peaks are detected for through-space dipolar coupled ^{1}H-^{1}H pairs within 5 Å distance. A detailed analysis of DQ-SQ spectra of black, partially transformed and yellow phases is given in SI (Figure S11). For the moisture exposed α|δ-$FAPbI_3$ sample (Figure 3d), a set of on- and off-diagonal DQ peaks at 14.8 and 15.6 ppm (gray box) corresponding to the ^{1}H sites in NH_2 and intra/intermolecular dipolar-coupled CH↔NH_2 sites of α-$FAPbI_3$ (intra- and intermolecular H-H distances are ≈4.54 Å and ≈2.28 Å) are detected. In addition, on- and off-diagonal DQ peaks at 17.0 and 16.1 ppm (yellow box) corresponding to the same moieties in δ-$FAPbI_3$ are observed. If FA^+ cations in the black and yellow phases were intermingled, the DQ-SQ spectrum would show a signal at 8.2+8.5 = 16.7 ppm, however, there is no DQ peak at this frequency (Figure 3d, dashed oval). This is due to fast reorientational motions of FA^+ cations in α– $FAPbI_3$ phase that partially average out dipole-dipole interactions or due to the flexible heterogenous interface between the phase-separated black and yellow regions or both of these combined.

Extending beyond the ^{1}H DQ-SQ NMR length scales (5 Å), 2D ^{1}H-^{1}H spin-diffusion (SD) experiment allows the magnetization exchange to occur between dipolar coupled ^{1}H-^{1}H sites within and beyond a nanometer distance to be probed. Specifically, the spin magnetization exchange between chemically inequivalent and dipolar coupled protons manifests as off-diagonal peaks. A detailed analysis of 2D ^{1}H-^{1}H SD spectra of $FAPbI_3$ before and after exposure to moisture acquired with various mixing times, τ_{mix}, is presented in SI (Figure S12). For the α|δ-$FAPbI_3$, there are no off-diagonal peaks between –CH (α-$FAPbI_3$) and –CH (δ-$FAPbI_3$) signals in the 2D spin diffusion spectrum (Figure 3e, dashed burgundy circles), indicating that there is no magnetization exchange between FA^+ cations in the black and yellow phases. This corroborates the above ssNMR analyses and confirms that the α and δ $FAPbI_3$ domains are locally phase segregated (micrograph,

Figure 3a), indicating that the structural transition occurs through a flexible and heterogeneous interface.[62] This leads us to investigate the dynamic behavior of organic cations in the α|δ-$FAPbI_3$ phase. For example, site-specific dynamics of organic cations have been previously studied by ssNMR and other complementary techniques.[42,46,63–67]

We introduce an *in situ* deuteration strategy that enables deuteration of FA^+ cations during the phase transformation. Upon exposure of α–$FAPbI_3$ to D_2O, the hydrogen atoms of NH_2 groups in FA cations exchange with deuterium sites, which can be achieved on-the-fly during the exposure to moisture (see Experimental section). The degree of deuteration in the converted δ–$FAPbI_3$ phase is estimated to be ~70% based on the quantitative 1D ^{1}H NMR measurements and analysis (SI, Figures S13, and S14). Insight into the dynamics of FA^+ cations in perovskite and non-perovskite phases were then obtained by analyzing ^{2}H NMR spectra of fresh and aged $FAPbI_3$ materials (Figure 4), whereby ^{2}H lineshape is sensitive to the local mobility and dynamic nature of the local ND_2 groups in black and yellow phases, and surface adsorbed D_2O molecules.[68–70] 1D ^{2}H spectrum of $FAPbI_3$ treated with D_2O (6 h, 85% RH) shows a peak at ~7.4 ppm corresponding to ND_2 sites in the black phase of FA^+ cations as well as minuscule concentration of D_2O molecules ingress at the grain boundaries, both of these undergo fast re-orientational motions at the NMR time scales leading to a narrow signal. To test this, a ^{2}H spectrum of liquid D_2O is acquired and compared, which showed a narrow signal at ~4.8 ppm due to the fast reorientational motion of D_2O molecules. Particularly interesting feature is that the same material after exposure to D_2O for 20 h displays different quadrupolar splittings (detected at much higher intensities for the $FAPbI_3$ after 68 h exposure to D_2O), which are simulated to obtain the quadrupolar constants (C_Q) of 53 and 81 kHz. This is in accord with the ^{2}H NMR spectra of control samples: a neat δ-$FAPbI_3$ material after exposure to D_2O displays identical lineshape and quadrupolar splitting (Figure 4, Figure S15), and

a neat cubic $FAPbBr_3$ as a control material (since it does not undergo a moisture induced phase transition) exhibits a narrow ^2H NMR feature (SI, Figure S16). It can be reasoned that these two different quadrupolar splittings correspond to relatively slow re-orientational motion of ND_2 sites of FA^+ cations in the yellow phase; one that corresponds to ND_2 sites facing toward the face-shared lead octahedra at the organic-inorganic interfaces, and the other corresponds to the ND_2 sites at the organic-organic (FA^+/FA^+) interface in between the chain-like lead octahedra. This suggests that the phase transformation occurs at the grain boundaries of the black phase triggered by the D_2O ingression that transforms into the yellow phase, whereby the trapped water molecules (if any) and FA^+ cations in the black $FAPbI_3$ particles at sub-surface layers undergo relatively fast reorientational motion than the NMR timescales and are likely to exhibit a flexible "liquid-like" interface. This is also consisted with the first-order reaction kinetics. While further investigation is required to quantify the prevalence and impact of moisture on the $\alpha \rightarrow \delta$ phase transformation at sub-grain boundaries, the results presented here show that a multinuclear (^1H, ^2H, ^{207}Pb) NMR spectroscopy can provide a powerful and non-destructive way of probing phase transformations and characterizing the $\alpha|\delta$-$FAPbI_3$ phase.

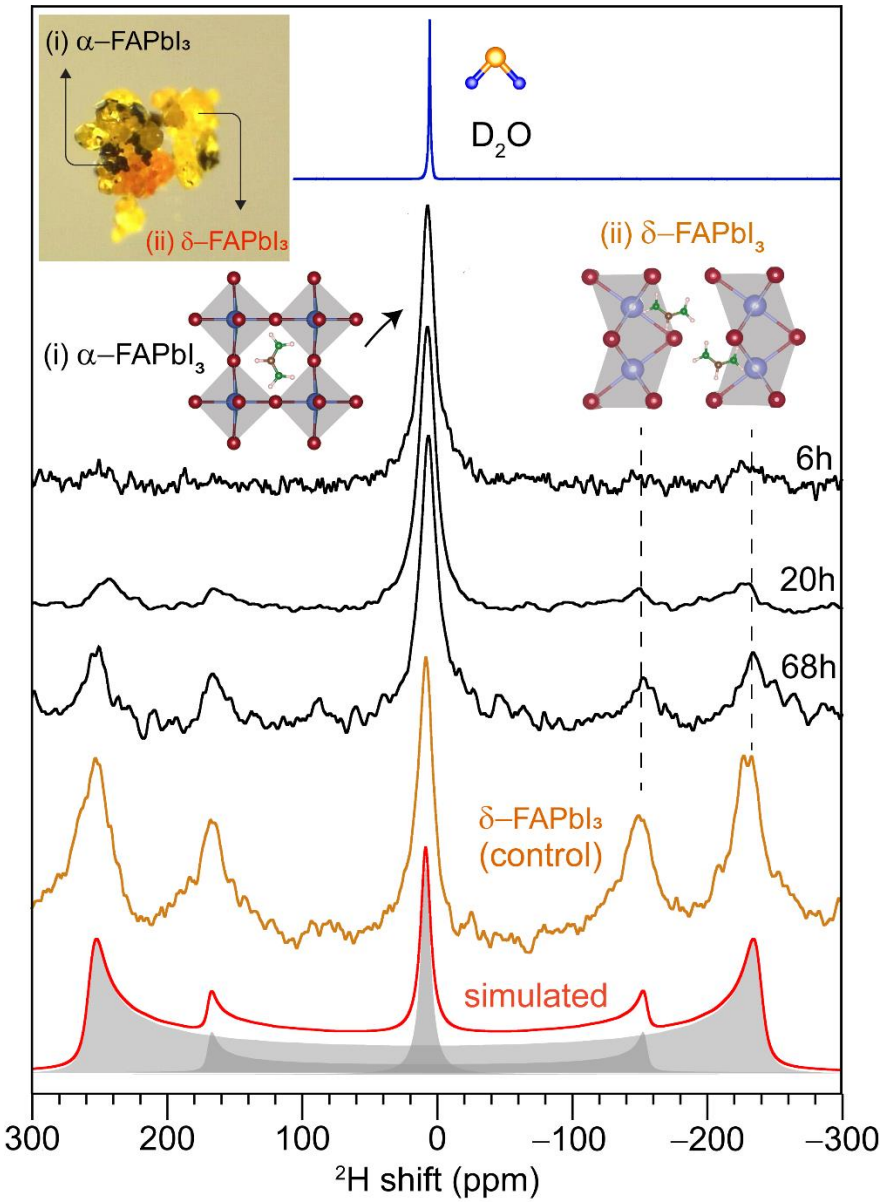

Figure 4. Solid-state static 1D ^{2}H NMR spectra of $FAPbI_3$ acquired at room temperature as a function of exposure time to D_2O vapor (85% RH) together with the 1D ^{2}H NMR spectrum of liquid D_2O acquired under the same conditions. A static ^{2}H NMR spectrum of control δ–$FAPbI_3$ material obtained after exposure to D_2O for 48h is acquired and compared. All spectra were acquired at 18.8 T (^{2}H = 122.8 MHz) and at room temperature. Inset on top is an optical microscopy image of a partially transformed $FAPbI_3$ crystal displaying the black and yellow regions at intra-grain interfaces.

In contrast to $FAPbI_3$, $FAPbBr_3$ exhibits enhanced moisture stability for several weeks, as revealed by combined XRD and ssNMR analysis. The experimental and simulated XRD powder patterns, shown in Figure 5a, indicate the phase purity in bulk. The formability and stability of hybrid perovskites depend on the Goldschmidt tolerance factor (*t*), with *t* values between 0.8 and 1.0 favoring the formation of cubic perovskite structures: $FAPbI_3$ and $FAPbBr_3$ exhibited *t* values of ~0.88 and ~0.90, leading to different phase stabilities.[71–73] A theoretical study corroborates that the $FAPbBr_3$ shows a greater extent of hydrogen bonding interactions than $FAPbI_3$.[74] The high field ^1H MAS NMR data of $FAPbI_3$ and $FAPbBr_3$ confirms this trend: for $FAPbBr_3$ the ^1H peaks are observed at higher frequencies (Figure 5b: NH_2 and CH peaks at 7.7 and 8.3 ppm) indicating stronger hydrogen bonding interactions than the α-$FAPbI_3$ that displays peaks at lower frequencies (Figure 1d: NH_2 and CH peaks at 7.4 and 8.1 ppm). 1D ^{207}Pb MAS spectrum (Figure 5c) of fresh $FAPbBr_3$ shows a ^{207}Pb signal centered at ~551 ppm corresponds to Pb atoms in a cubic phase,[75] and this signal after exposure to moisture (85% RH, 7 days) retained its position, suggesting that the moisture has little impact on the local structures of lead octahedra. In addition, a static ^2H NMR spectrum of $FAPbBr_3$ after exposure to D_2O (SI, Figure S15) shows a narrow feature centered at ~7.7 ppm, suggesting the fast reorientational motion of FA^+ cations in the cubic phase. Identical 1D ^1H and 2D ^1H-^1H DQ-SQ (Figures 5b, S17) spectral patterns of fresh and aged (85% RH, 7 days) powders further confirmed the enhanced environmental stability of $FAPbBr_3$ material.

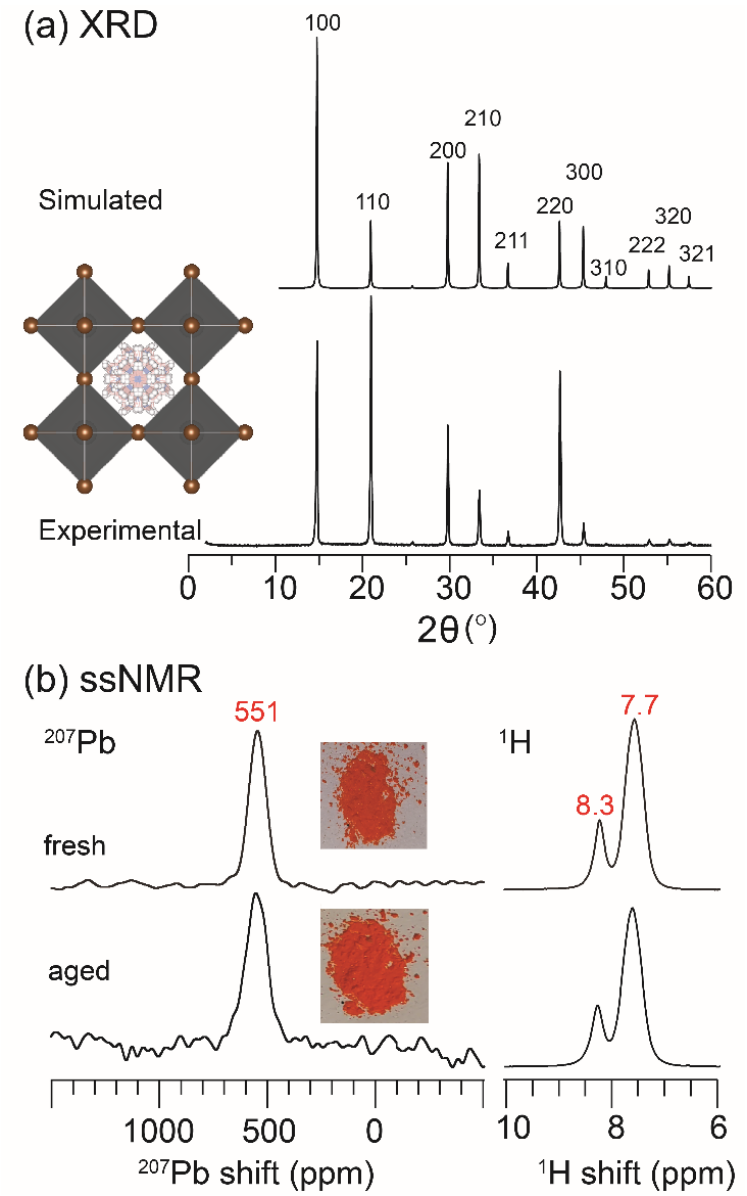

Figure 5. (a) Powder X-ray diffraction patterns of experimental and simulated $FAPbBr_3$. Solid-state (b) 1D ^{207}Pb (c) ^{1}H NMR spectra of fresh and aged $FAPbBr_3$ acquired at 50 kHz MAS frequency together with photographs taken before and after exposure to moisture for 7 days (85% RH).

Several aspects of the molecular-level understanding of transformative and reconstructive reactions in $FAPbX_3$ (X=I, Br) have been elucidated, including the kinetics of degradation reactions at grain/sub-grain boundaries as functions of water vapor concentration, particle size,

and light illumination, as well as the chemical nature of the α|δ-$FAPbI_3$ phase. Using combined time-resolved XRD and ssNMR spectroscopy, we unraveled the reaction kinetics of moisture-assisted structural transformations. Our results indicate that the cubic phase of $FAPbI_3$ is kinetically stable, whilst the cubic phase of $FAPbBr_3$ is thermodynamically stable at ambient temperatures with a wide range of humidity levels and exposure times in agreement with the recent study.[76] The half-lives of α-$FAPbI_3$, intra-grain morphology and chemical nature of intermediate species characterized at different length scales provide rich mechanistic insights. The key takeaway from this study is that the ambient stability of the black $FAPbI_3$ phase strongly depends on the external stimuli and kinetics of degradation reactions at the grain and sub-grain boundaries; a combination of these effects leads to variation of the transformation time from days to several months, or even a year. The reaction process that enables the transformation from the black phase to the yellow phase involves the surface-initiated local dissolution and precipitation mechanism, with water being the solvent. The synergy of multi-scale characterization techniques that are complementary with respect to each other and on-the-fly deuteration of organic cations demonstrated in this study is likely to be an essential feature of the strategies to understand the transformative reactions in hybrid halide perovskites and develop interfacial engineering strategies in the future. This study also suggests that the single crystal $FAPbI_3$ and FA-rich materials provide a path forward for stable and efficient optoelectronics.

Associated Content

Materials and methods, powder XRD patterns of $FAPbI_3$, SEM micrograms, HR optical microscopy images, 1D ^{1}H MAS, kinetics plots, data fitting and 2D ^{1}H-^{1}H DQ-SQ and 2D ^{1}H spin

diffusion NMR spectra, ^{2}H and ^{1}H lineshape analyses of $FAPbI_3$. 1D static ^{2}H and ^{1}H lineshape analyses, 1D ^{1}H, ^{2}H, and 2D ^{1}H-^{1}H MAS NMR spectra of $FAPbBr_3$.

Present address

[¤]Department of Chemistry, University of South Florida, Tampa, FL, 33620

Conflict of Interest

Authors declare no conflict of interest.

Acknowledgements

At Northwestern University and UCSB, this work is mainly supported by the Department of Energy, Office of Science, Basic Energy Sciences, under Grant No. SC0012541 (synthesis, structure, and characterization of physical properties). The research reported here also made use the shared facilities of the UCSB MRSEC (National Science Foundation DMR 1720256), a member of the Materials Research Facilities Network (www.mrfn.org). R.M.K. gratefully acknowledges the National Defense Science and Engineering Graduate fellowship for financial support. G. N. M. R. and P. R. acknowledge the funding from University of Lille and region Hauts-de-France (HDF), and the support from the IR-RMN-THC FR-3050 CNRS France for conducting ssNMR measurements. G. N. M. R. acknowledges the funding from EU-H2020 research and innovation programme under the Marie Skłodowska-Curie grant no. 795091.

References

(1) Eperon, G. E.; Hörantner, M. T.; Snaith, H. J. Metal Halide Perovskite Tandem and

Multiple-Junction Photovoltaics. *Nat. Rev. Chem.* **2017**, *1*, 1–18.

(2) Manser, J. S.; Christians, J. A.; Kamat, P. V. Intriguing Optoelectronic Properties of Metal Halide Perovskites. *Chem. Rev.* **2016**, *116*, 12956–13008.

(3) Liu, X. K.; Xu, W.; Bai, S.; Jin, Y.; Wang, J.; Friend, R. H.; Gao, F. Metal Halide Perovskites for Light-Emitting Diodes. *Nat. Mater.* **2021**, *20*, 10–21.

(4) Lee, M. M.; Teuscher, J.; Miyasaka, T.; Murakami, T. N.; Snaith, H. J. Efficient Hybrid Solar Cells Based on Meso-Superstructured Organometal Halide Perovskites. *Science* **2012**, *338*, 643–647.

(5) Xing, G.; Mathews, N.; Sun, S.; Lim, S. S.; Lam, Y. M.; Graẗzel, M.; Mhaisalkar, S.; Sum, T. C. Long-Range Balanced Electron-and Hole-Transport Lengths in Organic-Inorganic $CH_3NH_3PbI_3$. *Science* **2013**, *342*, 344–347.

(6) Stranks, S. D.; Eperon, G. E.; Grancini, G.; Menelaou, C.; Alcocer, M. J. P.; Leijtens, T.; Herz, L. M.; Petrozza, A.; Snaith, H. J. Electron-Hole Diffusion Lengths Exceeding 1 Micrometer in an Organometal Trihalide Perovskite Absorber. *Science* **2013**, *342*, 341–344.

(7) Stoumpos, C. C.; Malliakas, C. D.; Kanatzidis, M. G. Semiconducting Tin and Lead Iodide Perovskites with Organic Cations: Phase Transitions, High Mobilities, and near-Infrared Photoluminescent Properties. *Inorg. Chem.* **2013**, *52*, 9019–9038.

(8) Bryant, D.; Aristidou, N.; Pont, S.; Sanchez-Molina, I.; Chotchunangatchaval, T.; Wheeler, S.; Durrant, J. R.; Haque, S. A. Light and Oxygen Induced Degradation Limits the Operational Stability of Methylammonium Lead Triiodide Perovskite Solar Cells. *Energy Environ. Sci.* **2016**, *9*, 1655–1660.

(9) Ma, L.; Guo, D.; Li, M.; Wang, C.; Zhou, Z.; Zhao, X.; Zhang, F.; Ao, Z.; Nie, Z. Temperature-Dependent Thermal Decomposition Pathway of Organic-Inorganic Halide

Perovskite Materials. *Chem. Mater.* **2019**, *31*, 8515–8522.

(10) Kundu, S.; Kelly, T. L. In Situ Studies of the Degradation Mechanisms of Perovskite Solar Cells. *EcoMat* **2020**, *2*, e12025.

(11) Grancini, G.; Nazeeruddin, M. K. Dimensional Tailoring of Hybrid Perovskites for Photovoltaics. *Nat. Rev. Mater.* **2018**, *4*, 4–22.

(12) Masi, S.; Gualdrón-Reyes, A. F.; Mora-Seró, I. Stabilization of Black Perovskite Phase in $FAPbI_3$ and $CsPbI_3$. *ACS Energy Lett.* **2020**, *5*, 1974–1985.

(13) Fan, Y.; Meng, H.; Wang, L.; Pang, S. Review of Stability Enhancement for Formamidinium-Based Perovskites. *Sol. RRL* **2019**, *3*, 1900215.

(14) Saidaminov, M. I.; Kim, J.; Jain, A.; Quintero-Bermudez, R.; Tan, H.; Long, G.; Tan, F.; Johnston, A.; Zhao, Y.; Voznyy, O.; Sargent, E. H. Suppression of Atomic Vacancies via Incorporation of Isovalent Small Ions to Increase the Stability of Halide Perovskite Solar Cells in Ambient Air. *Nat. Energy* **2018**, *3*, 648–654.

(15) Jeong, J.; Kim, M.; Seo, J.; Lu, H.; Ahlawat, P.; Mishra, A.; Yang, Y.; Hope, M. A.; Eickemeyer, F. T.; Kim, M.; Yoon, Y. J.; Choi, I. W.; Darwich, B. P.; Choi, S. J.; Jo, Y.; Lee, J. H.; Walker, B.; Zakeeruddin, S. M.; Emsley, L.; Rothlisberger, U.; Hagfeldt, A.; Kim, D. S.; Grätzel, M.; Kim, J. Y. Pseudo-Halide Anion Engineering for α-$FAPbI_3$ Perovskite Solar Cells. *Nature* **2021**, *592*, 381–385.

(16) Jiang, Q.; Zhao, Y.; Zhang, X.; Yang, X.; Chen, Y.; Chu, Z.; Ye, Q.; Li, X.; Yin, Z.; You, J. Surface Passivation of Perovskite Film for Efficient Solar Cells. *Nat. Photonics* **2019**, *13*, 460–466.

(17) Zheng, X.; Hou, Y.; Bao, C.; Yin, J.; Yuan, F.; Huang, Z.; Song, K.; Liu, J.; Troughton, J.; Gasparini, N.; Zhou, C.; Lin, Y.; Xue, D.-J.; Chen, B.; Johnston, A. K.; Wei, N.; Hedhili,

M. N.; Wei, M.; Alsalloum, A. Y.; Maity, P.; Turedi, B.; Yang, C.; Baran, D.; Anthopoulos, T. D.; Han, Y.; Lu, Z.-H.; Mohammed, O. F.; Gao, F.; Sargent, E. H.; Bakr, O. M. Managing Grains and Interfaces via Ligand Anchoring Enables 22.3%-Efficiency Inverted Perovskite Solar Cells. *Nat. Energy* **2020**, *5*, 131–140.

(18) Jung, E. H.; Jeon, N. J.; Park, E. Y.; Moon, C. S.; Shin, T. J.; Yang, T.-Y.; Noh, J. H.; Seo, J. Efficient, Stable and Scalable Perovskite Solar Cells Using Poly(3-Hexylthiophene). *Nature* **2019**, *567*, 511–515.

(19) Salim, K. M. M.; Masi, S.; Gualdrón-Reyes, A. F.; Sánchez, R. S.; Barea, E. M.; Krečmarová, M.; Sánchez-Royo, J. F.; Mora-Seró, I. Boosting Long-Term Stability of Pure Formamidinium Perovskite Solar Cells by Ambient Air Additive Assisted Fabrication. *ACS Energy Lett.* **2021**, *10*, 3511–3521.

(20) Chen, J.; He, D.; Park, N. G. Methodologies for >30% Efficient Perovskite Solar Cells via Enhancement of Voltage and Fill Factor. *Sol. RRL* **2022**, *6*, 2100767.

(21) IEC 61215-1:2016 | IEC Webstore | rural electrification, solar power, solar panel, photovoltaic, PV, smart city, LVDC https://webstore.iec.ch/publication/24312 (accessed Sep 20, 2021).

(22) Cheacharoen, R.; Boyd, C. C.; Burkhard, G. F.; Leijtens, T.; Raiford, J. A.; Bush, K. A.; Bent, S. F.; McGehee, M. D. Encapsulating Perovskite Solar Cells to Withstand Damp Heat and Thermal Cycling. *Sustain. Energy Fuels* **2018**, *2*, 2398–2406.

(23) Cheacharoen, R.; Rolston, N.; Harwood, D.; Bush, K. A.; Dauskardt, R. H.; McGehee, M. D. Design and Understanding of Encapsulated Perovskite Solar Cells to Withstand Temperature Cycling. *Energy Environ. Sci.* **2018**, *11*, 144–150.

(24) Bush, K. A.; Palmstrom, A. F.; Yu, Z. J.; Boccard, M.; Cheacharoen, R.; Mailoa, J. P.;

McMeekin, D. P.; Hoye, R. L. Z.; Bailie, C. D.; Leijtens, T.; Peters, I. M.; Minichetti, M. C.; Rolston, N.; Prasanna, R.; Sofia, S.; Harwood, D.; Ma, W.; Moghadam, F.; Snaith, H. J.; Buonassisi, T.; Holman, Z. C.; Bent, S. F.; McGehee, M. D. 23.6%-Efficient Monolithic Perovskite/Silicon Tandem Solar Cells with Improved Stability. *Nat. Energy* **2017**, *2*, 1–7.

(25) Nair, S.; Gohel, J. V. A Study on Optoelectronic Performance of Perovskite Solar Cell under Different Stress Testing Conditions. *Opt. Mater.* **2020**, *109*, 110377.

(26) Min, H.; Lee, D. Y.; Kim, J.; Kim, G.; Lee, K. S.; Kim, J.; Paik, M. J.; Kim, Y. K.; Kim, K. S.; Kim, M. G.; Shin, T. J.; Il Seok, S. Perovskite Solar Cells with Atomically Coherent Interlayers on SnO_2 Electrodes. *Nature* **2021**, *598*, 444–450.

(27) Hui, W.; Chao, L.; Lu, H.; Xia, F.; Wei, Q.; Su, Z.; Niu, T.; Tao, L.; Du, B.; Li, D.; Wang, Y.; Zuo, S.; Li, B.; Shi, W.; Ran, X.; Li, P.; Zhang, H.; Wu, Z.; Ran, C.; Song, L.; Xing, G.; Gao, X.; Zhang, J.; Xia, Y.; Chen, Y.; Huang, W. Stabilizing Black-Phase Formamidinium Perovskite Formation at Room Temperature and High Humidity. *Science.* **2021**, *371*, 1359–1364.

(28) Park, B. wook; Kwon, H. W.; Lee, Y.; Lee, D. Y.; Kim, M. G.; Kim, G.; Kim, K. jeong; Kim, Y. K.; Im, J.; Shin, T. J.; Seok, S. Il. Stabilization of Formamidinium Lead Triiodide α-Phase with Isopropylammonium Chloride for Perovskite Solar Cells. *Nat. Energy* **2021**, *6*, 419–428.

(29) Liu, Y.; Akin, S.; Hinderhofer, A.; Eickemeyer, F. T.; Zhu, H.; Seo, J.; Zhang, J.; Schreiber, F.; Zhang, H.; Zakeeruddin, S. M.; Hagfeldt, A.; Dar, M. I.; Grätzel, M. Stabilization of Highly Efficient and Stable Phase-Pure $FAPbI_3$ Perovskite Solar Cells by Molecularly Tailored 2D-Overlayers. *Angew. Chemie* **2020**, *132*, 15818–15824.

(30) Li, Y.; Liu, F. Z.; Waqas, M.; Leung, T. L.; Tam, H. W.; Lan, X. Q.; Tu, B.; Chen, W.;

Djurišić, A. B.; He, Z. B. Formamidinium-Based Lead Halide Perovskites: Structure, Properties, and Fabrication Methodologies. *Small Methods* **2018**, *2*, 1700387.

(31) Doherty, T. A. S.; Nagane, S.; Kubicki, D. J.; Jung, Y.-K.; Johnstone, D. N.; Iqbal, A. N.; Guo, D.; Frohna, K.; Danaie, M.; Tennyson, E. M.; Macpherson, S.; Abfalterer, A.; Anaya, M.; Chiang, Y.-H.; Crout, P.; Ruggeri, F. S.; Collins, S. M.; Grey, C. P.; Walsh, A.; Midgley, P. A.; Stranks, S. D. Stabilized Tilted-Octahedra Halide Perovskites Inhibit Local Formation of Performance-Limiting Phases. *Science.* **2021**, *374*, 1598–1605.

(32) Binek, A.; Hanusch, F. C.; Docampo, P.; Bein, T. Stabilization of the Trigonal High-Temperature Phase of Formamidinium Lead Iodide. *J. Phys. Chem. Lett.* **2015**, *6*, 1249–1253.

(33) Kim, S.; Eom, T.; Ha, Y.-S.; Hong, K.-H.; Kim, H. Thermodynamics of Multicomponent Perovskites: A Guide to Highly Efficient and Stable Solar Cell Materials. *Chem. Mater.* **2020**, *32*, 4265–4272.

(34) Qiu, W.; Ray, A.; Jaysankar, M.; Merckx, T.; Bastos, J. P.; Cheyns, D.; Gehlhaar, R.; Poortmans, J.; Heremans, P. An Interdiffusion Method for Highly Performing Cesium/Formamidinium Double Cation Perovskites. *Adv. Funct. Mater.* **2017**, *27*, 1700920.

(35) Chen, T.; Foley, B. J.; Park, C.; Brown, C. M.; Harriger, L. W.; Lee, J.; Ruff, J.; Yoon, M.; Choi, J. J.; Lee, S. H. Entropy-Driven Structural Transition and Kinetic Trapping in Formamidinium Lead Iodide Perovskite. *Sci. Adv.* **2016**, *2*, e1601650.

(36) Cordero, F.; Craciun, F.; Trequattrini, F.; Generosi, A.; Paci, B.; Paoletti, A. M.; Pennesi, G. Stability of Cubic $FAPbI_3$ from X-Ray Diffraction, Anelastic, and Dielectric Measurements. *J. Phys. Chem. Lett.* **2019**, *10*, 2463–2469.

(37) Cordero, F.; Craciun, F.; Trequattrini, F.; Generosi, A.; Paci, B.; Paoletti, A. M.; Zanotti,

G. Influence of Temperature, Pressure, and Humidity on the Stabilities and Transition Kinetics of the Various Polymorphs of $FAPbI_3$. *J. Phys. Chem. C* **2020**, *124*, 22972–22980.

(38) Han, Q.; Bae, S.-H.; Sun, P.; Hsieh, Y.-T.; Yang, Y. M.; Rim, Y. S.; Zhao, H.; Chen, Q.; Shi, W.; Li, G.; Yang, Y. Single Crystal Formamidinium Lead Iodide ($FAPbI_3$): Insight into the Structural, Optical, and Electrical Properties. *Adv. Mater.* **2016**, *28*, 2253–2258.

(39) Steele, J. A.; Yuan, H.; Tan, C. Y. X.; Keshavarz, M.; Steuwe, C.; Roeffaers, M. B. J.; Hofkens, J. Direct Laser Writing of δ- To α-Phase Transformation in Formamidinium Lead Iodide. *ACS Nano* **2017**, *11*, 8072–8083.

(40) Zheng, H.; Duan, J.; Dai, J. Synthesis of Formamidinium Lead Iodide Perovskite Bulk Single Crystal and Its Optical Properties. *Int. J. Mod. Phys. B* **2017**, *31*, 1744066.

(41) Ho, K.; Wei, M.; Sargent, E. H.; Walker, G. C. Grain Transformation and Degradation Mechanism of Formamidinium and Cesium Lead Iodide Perovskite under Humidity and Light. *ACS Energy Lett.* **2021**, *6*, 934–940.

(42) Kubicki, D. J.; Stranks, S. D.; Grey, C. P.; Emsley, L. NMR Spectroscopy Probes Microstructure, Dynamics and Doping of Metal Halide Perovskites. *Nat. Rev. Chem.* **2021**, *5*, 624–645.

(43) Dahlman, C. J.; Kubicki, D. J.; Reddy, G. N. M. Interfaces in Metal Halide Perovskites Probed by Solid-State NMR Spectroscopy. *J. Mater. Chem. A* **2021**, *9*, 19206–19244.

(44) Askar, A. M.; Bernard, G. M.; Wiltshire, B.; Shankar, K.; Michaelis, V. K. Multinuclear Magnetic Resonance Tracking of Hydro, Thermal, and Hydrothermal Decomposition of $CH_3NH_3PbI_3$. *J. Phys. Chem. C* **2017**, *121*, 1013–1024.

(45) Franssen, W. M. J.; Kentgens, A. P. M. Solid–State NMR of Hybrid Halide Perovskites. *Solid State Nucl. Magn. Reson.* **2019**, *100*, 36–44.

(46) Grüninger, H.; Bokdam, M.; Leupold, N.; Tinnemans, P.; Moos, R.; De Wijs, G. A.; Panzer, F.; Kentgens, A. P. M. Microscopic (Dis)Order and Dynamics of Cations in Mixed FA/MA Lead Halide Perovskites. *J. Phys. Chem. C* **2021**, *125*, 1742–1753.

(47) Kazemi, M. A. A.; Raval, P.; Cherednichekno, K.; Chotard, J.-N.; Krishna, A.; Demortiere, A.; Reddy, G. N. M.; Sauvage, F. Molecular-Level Insight into Correlation between Surface Defects and Stability of Methylammonium Lead Halide Perovskite Under Controlled Humidity. *Small Methods* **2021**, *5*, 2000834.

(48) Rosales, B. A.; Men, L.; Cady, S. D.; Hanrahan, M. P.; Rossini, A. J.; Vela, J. Persistent Dopants and Phase Segregation in Organolead Mixed-Halide Perovskites. *Chem. Mater.* **2016**, *28*, 6848–6859.

(49) Ali, J.; Li, Y.; Gao, P.; Hao, T.; Song, J.; Zhang, Q.; Zhu, L.; Wang, J.; Feng, W.; Hu, H.; Liu, F. Interfacial and Structural Modifications in Perovskite Solar Cells. *Nanoscale* **2020**, *12*, 5719–5745.

(50) Weller, M. T.; Weber, O. J.; Frost, J. M.; Walsh, A. Cubic Perovskite Structure of Black Formamidinium Lead Iodide, α-$[HC(NH_2)_2]PbI_3$, at 298 K. *J. Phys. Chem. Lett.* **2015**, *6*, 3209–3212.

(51) Lee, J.; Lee, W.; Kang, K.; Lee, T.; Lee, S. K. Layer-by-Layer Structural Identification of 2D Ruddlesden–Popper Hybrid Lead Iodide Perovskites by Solid-State NMR Spectroscopy. *Chem. Mater.* **2021**, *33*, 370–377.

(52) Hanrahan, M. P.; Men, L.; Rosales, B. A.; Vela, J.; Rossini, A. J. Sensitivity-Enhanced ^{207}Pb Solid-State NMR Spectroscopy for the Rapid, Non-Destructive Characterization of Organolead Halide Perovskites. *Chem. Mater.* **2018**, *30*, 7005–7015.

(53) Febriansyah, B.; Koh, T. M.; Rana, P. J. S.; Hooper, T. J. N.; Ang, Z. Z.; Li, Y.; Bruno, A.;

Grätzel, M.; England, J.; Mhaisalkar, S. G.; Mathews, N. Hybrid 2D $[Pb(CH_3NH_2)I_2]_n$ Coordination Polymer Precursor for Scalable Perovskite Deposition. *ACS Energy Lett.* **2020**, *5*, 2305–2312.

(54) Li, W.; Rothmann, M. U.; Zhu, Y.; Chen, W.; Yang, C.; Yuan, Y.; Choo, Y. Y.; Wen, X.; Cheng, Y. B.; Bach, U.; Etheridge, J. The Critical Role of Composition-Dependent Intragrain Planar Defects in the Performance of $MA_{1-x}FA_xPbI_3$ Perovskite Solar Cells. *Nat. Energy* **2021**, *6*, 624–632.

(55) Yun, J. S.; Kim, J.; Young, T.; Patterson, R. J.; Kim, D.; Seidel, J.; Lim, S.; Green, M. A.; Huang, S.; Ho-Baillie, A. Humidity-Induced Degradation via Grain Boundaries of $HC(NH_2)_2PbI_3$ Planar Perovskite Solar Cells. *Adv. Funct. Mater.* **2018**, *28*, 1705363.

(56) Park, Y. H.; Jeong, I.; Bae, S.; Son, H. J.; Lee, P.; Lee, J.; Lee, C.-H.; Ko, M. J. Inorganic Rubidium Cation as an Enhancer for Photovoltaic Performance and Moisture Stability of $HC(NH_2)_2PbI_3$ Perovskite Solar Cells. *Adv. Funct. Mater.* **2017**, *27*, 1605988.

(57) Ono, L. K.; Juarez-Perez, E. J.; Qi, Y. Progress on Perovskite Materials and Solar Cells with Mixed Cations and Halide Anions. *ACS Appl. Mater. Interfaces* **2017**, *9*, 30197–30246.

(58) Smecca, E.; Numata, Y.; Deretzis, I.; Pellegrino, G.; Boninelli, S.; Miyasaka, T.; Magna, A. La; Alberti, A. Stability of Solution-Processed $MAPbI_3$ and $FAPbI_3$ Layers. *Phys. Chem. Chem. Phys.* **2016**, *18*, 13413–13422.

(59) Zhang, T.; Meng, X.; Bai, Y.; Xiao, S.; Hu, C.; Yang, Y.; Chen, H.; Yang, S. Profiling the Organic Cation-Dependent Degradation of Organolead Halide Perovskite Solar Cells. *J. Mater. Chem. A* **2017**, *5*, 1103–1111.

(60) Bischak, C. G.; Lai, M.; Fan, Z.; Lu, D.; David, P.; Dong, D.; Chen, H.; Etman, A. S.; Lei, T.; Sun, J.; Grünwald, M.; Limmer, D. T.; Yang, P.; Ginsberg, N. S. Liquid-like Interfaces

Mediate Structural Phase Transitions in Lead Halide Perovskites. *Matter* **2020**, *3*, 534–545.

(61) Xue, J.; Wang, R.; Wang, K. L.; Wang, Z. K.; Yavuz, I.; Wang, Y.; Yang, Y.; Gao, X.; Huang, T.; Nuryyeva, S.; Lee, J. W.; Duan, Y.; Liao, L. S.; Kaner, R.; Yang, Y. Crystalline Liquid-like Behavior: Surface-Induced Secondary Grain Growth of Photovoltaic Perovskite Thin Film. *J. Am. Chem. Soc.* **2019**, *141*, 13948–13953.

(62) Yun, J. S.; Kim, J.; Young, T.; Patterson, R. J.; Kim, D.; Seidel, J.; Lim, S.; Green, M. A.; Huang, S.; Ho-Baillie, A. Humidity-Induced Degradation via Grain Boundaries of $HC(NH_2)_2PbI_3$ Planar Perovskite Solar Cells. *Adv. Funct. Mater.* **2018**, *28*, 1705363.

(63) Piveteau, L.; Morad, V.; Kovalenko, M. V. Solid-State NMR and NQR Spectroscopy of Lead-Halide Perovskite Materials. *J. Am. Chem. Soc.* **2020**, *142*, 19413–19437.

(64) Mozur, E. M.; Hope, M. A.; Trowbridge, J. C.; Halat, D. M.; Daemen, L. L.; Maughan, A. E.; Prisk, T. R.; Grey, C. P.; Neilson, J. R. Cesium Substitution Disrupts Concerted Cation Dynamics in Formamidinium Hybrid Perovskites. *Chem. Mater.* **2020**, *32*, 6266–6277.

(65) Drużbicki, K.; Lavén, R.; Armstrong, J.; Malavasi, L.; Fernandez-Alonso, F.; Karlsson, M. Cation Dynamics and Structural Stabilization in Formamidinium Lead Iodide Perovskites. *J. Phys. Chem. Lett.* **2021**, *12*, 3503–3508.

(66) Fabini, D. H.; Siaw, T. A.; Stoumpos, C. C.; Laurita, G.; Olds, D.; Page, K.; Hu, J. G.; Kanatzidis, M. G.; Han, S.; Seshadri, R. Universal Dynamics of Molecular Reorientation in Hybrid Lead Iodide Perovskites. *J. Am. Chem. Soc.* **2017**, *139*, 16875–16884.

(67) Dahlman, C. J.; Kennard, R. M.; Paluch, P.; Venkatesan, N. R.; Chabinyc, M. L.; Manjunatha Reddy, G. N. Dynamic Motion of Organic Spacer Cations in Ruddlesden–Popper Lead Iodide Perovskites Probed by Solid-State NMR Spectroscopy. *Chem. Mater.* **2021**, *33*, 642–656.

(68) Knop, O.; Wasylishen, R. E.; Anne White, M.; Stanley Cameron, T.; M Van Oort, M. J. Alkylammonium Lead Halides. Part 2. $CH_3NH_3PbX_3$ (X = C1, Br, I) Perovskites: Cuboctahedral Halide Cages with Isotropic Cation Reorientation. *Can. J. Chem.* **1990**, *68*, 412.

(69) Kubicki, D. J.; Prochowicz, D.; Hofstetter, A.; Péchy, P.; Zakeeruddin, S. M.; Grätzel, M.; Emsley, L. Cation Dynamics in Mixed-Cation $(MA)_x(FA)_{1-x}PbI_3$ Hybrid Perovskites from Solid-State NMR. *J. Am. Chem. Soc.* **2017**, *139*, 10055–10061.

(70) Roiland, C.; Trippé-Allard, G.; Jemli, K.; Alonso, B.; Ameline, J. C.; Gautier, R.; Bataille, T.; Le Pollès, L.; Deleporte, E.; Even, J.; Katan, C. Multinuclear NMR as a Tool for Studying Local Order and Dynamics in $CH_3NH_3PbX_3$ (X = Cl, Br, I) Hybrid Perovskites. *Phys. Chem. Chem. Phys.* **2016**, *18*, 27133–27142.

(71) Li, Z.; Yang, M.; Park, J. S.; Wei, S. H.; Berry, J. J.; Zhu, K. Stabilizing Perovskite Structures by Tuning Tolerance Factor: Formation of Formamidinium and Cesium Lead Iodide Solid-State Alloys. *Chem. Mater.* **2016**, *28*, 284–292.

(72) Fan, Z.; Sun, K.; Wang, J. Perovskites for Photovoltaics: A Combined Review of Organic–Inorganic Halide Perovskites and Ferroelectric Oxide Perovskites. *J. Mater. Chem. A* **2015**, *3*, 18809–18828.

(73) Bartel, C. J.; Sutton, C.; Goldsmith, B. R.; Ouyang, R.; Musgrave, C. B.; Ghiringhelli, L. M.; Scheffler, M. New Tolerance Factor to Predict the Stability of Perovskite Oxides and Halides. *Sci. Adv.* **2019**, *5*, eaav0693.

(74) Svane, K. L.; Forse, A. C.; Grey, C. P.; Kieslich, G.; Cheetham, A. K.; Walsh, A.; Butler, K. T. How Strong Is the Hydrogen Bond in Hybrid Perovskites? *J. Phys. Chem. Lett.* **2017**, *8*, 6154–6159.

(75) Aebli, M.; Piveteau, L.; Nazarenko, O.; Benin, B. M.; Krieg, F.; Verel, R.; Kovalenko, M. V. Lead-Halide Scalar Couplings in ^{207}Pb NMR of $APbX_3$ Perovskites (A = Cs, Methylammonium, Formamidinium; X = Cl, Br, I). *Sci. Rep.* **2020**, *10*, 8229.

(76) Vasileiadou, E. S.; Hadar, I.; Kepenekian, M.; Even, J.; Tu, Q.; Malliakas, C. D.; Friedrich, D.; Spanopoulos, I.; Hoffman, J. M.; Dravid, V. P.; Kanatzidis, M. G. Shedding Light on the Stability and Structure-Property Relationships of Two-Dimensional Hybrid Lead Bromide Perovskites. *Chem. Mater.* **2021**, *33*, 5085–5107.